JOURNAL OF GEOPHYSICAL RESEARCH, VOL. 111, B06307, doi:10.1029/2005JB003973, 2006

A global study of transition zone thickness using receiver functions

Jesse F. Lawrence[1] and Peter M. Shearer[1]

Received 1 August 2005; revised 17 February 2006; accepted 28 February 2006; published 16 June 2006.

[1] Systematic stacks of *P* wave receiver functions (*Pds*) for 118 global seismic stations yield new transition zone thickness (W_{TZ}) estimates, as measured by the difference in depths between the 410- and 660-km mantle discontinuities. The receiver functions are computed from high signal-to-noise records of earthquakes between 1976 and 2002 recorded at distances of 30° to 90°. We obtain a globally averaged transition zone thickness of 242 ± 2 km, in good agreement with *SS* precursor (*SdS*) results. Previously noted differences in average W_{TZ} between *Pds* and *SdS* studies are caused by both geographic bias and the constant ray parameter approximation used in many prior *Pds* studies, which causes a ~4 km overestimation of W_{TZ}. *Pds* observations suggest lateral variations in W_{TZ} of ±20 km with maximal variations of ±35 km and a long-wavelength topography pattern that agrees with *SS* precursor results showing thick W_{TZ} beneath cold subduction zones and thin W_{TZ} beneath warmer regions.

Citation: Lawrence, J. F., and P. M. Shearer (2006), A global study of transition zone thickness using receiver functions, *J. Geophys. Res.*, *111*, B06307, doi:10.1029/2005JB003973.

1. Introduction

[2] The mantle transition zone (MTZ), bounded by discontinuities at ~410 and ~660 km depths, is thought to play a central role in controlling mantle flow [*Yuen et al.*, 1994]. Mineral physics experiments demonstrate that phase changes from olivine to β phase and γ-spinel to perovskite + magnesiowustite at pressures equivalent to 410 and 660 km likely explain the velocity jumps observed by seismologists [*Jackson*, 1983; *Ringwood*, 1975]. Temperature variations will cause thickening and thinning of the transition zone because of the positive and negative Clapeyron slopes for the 410- and 660-km discontinuities respectively [e.g., *Katsura and Ito*, 1989]. The most prominent techniques currently used to seismically observe the 410- and 660-km discontinuities are *SS* precursor (or *SdS*) analyses [*Shearer*, 1991, 1993; *Shearer and Masters*, 1992; *Gossler and Kind*, 1996; *Lee and Grand*, 1996; *Flanagan and Shearer*, 1998; *Gu et al.*, 1998; *Deuss and Woodhouse*, 2001, 2002; *Gu and Dziewonski*, 2002] and *P*-to-*S* conversion (or *Pds*) analyses [*Vinnik*, 1977; *Petersen et al.*, 1993; *Bostock*, 1996; *Shen et al.*, 1996; *Vinnik et al.*, 1996; *Dueker and Sheehan*, 1997; *Gurrola and Minster*, 1998; *Li et al.*, 1998; *Shen et al.*, 1998; *Chevrot et al.*, 1999; *Gilbert et al.*, 2003].

[3] *SS* precursors (*SdS*) are teleseismic shear waves that reflect from the underside of interfaces at depth *d*, having arrival times determined by the interface depth and the background seismic velocity structure (Figure 1). These precursors are sensitive to large X-shaped Fresnel zones surrounding the foci of the underside *SdS* reflections [e.g., *Shearer et al.*, 1999]. At distances between 110° and 180° the *SdS* arrivals may be stacked without interference from other phases, allowing for their analysis despite amplitudes in individual seismograms typically well below the ambient noise. *SS* precursor studies have good global coverage because of the wide distribution of *SS* bounce points, and indicate that the global average W_{TZ} is 242 ± 2 km with long-wavelength deviations of approximately ±20 km [*Flanagan and Shearer*, 1998; *Gu et al.*, 1998].

[4] Receiver function analyses yield more detailed measures of interface depths beneath seismic stations by isolating *Pds* arrivals, which result from teleseismic *P* waves that convert a portion of their energy into shear waves at interface depth *d* (Figure 1). *Pds* studies are sensitive to velocity and interface depth for small regions beneath three-component seismometers [e.g., *Langston*, 1979; *Ammon et al.*, 1990; *Ammon*, 1991; *Gurrola and Minster*, 1998]. Owing to the small scale of *Pds* sensitivity and the limited geographic distribution of seismometers, *Pds* is less suited for global-scale analysis than *SdS*. However, the 82 global *Pds* times compiled and calculated by *Chevrot et al.* [1999] indicated an average W_{TZ} that is globally ~8 km thicker than results of *SdS* studies and with poor correlation in observed values among different regions.

[5] Global studies of *SdS* repeatedly have shown long-wavelength variations of transition zone thickness consistent with thickening beneath subduction zones and parts of continents and thinning beneath oceanic plates and above the African and Pacific megaplumes [*Flanagan and Shearer*, 1998; *Gu et al.*, 1998; *Gu and Dziewonski*, 2002]. These studies stack *SS* precursors regionally by *SdS* bounce point. The pattern of thick and thin W_{TZ} agrees with mineral physics experiments that show opposite Clapeyron slopes at the 410- and 660-km discontinuities [e.g., *Katsura and Ito*, 1989]. These studies indicate thinner W_{TZ} in colder regions (subduction zones) and thicker W_{TZ} in warmer regions. The good agreement among different *SdS* studies [*Flanagan*

[1]Institute of Geophysics and Planetary Physics, Scripps Institution of Oceanography, La Jolla, California, USA.

0148-0227/06/2005JB003973$09.00

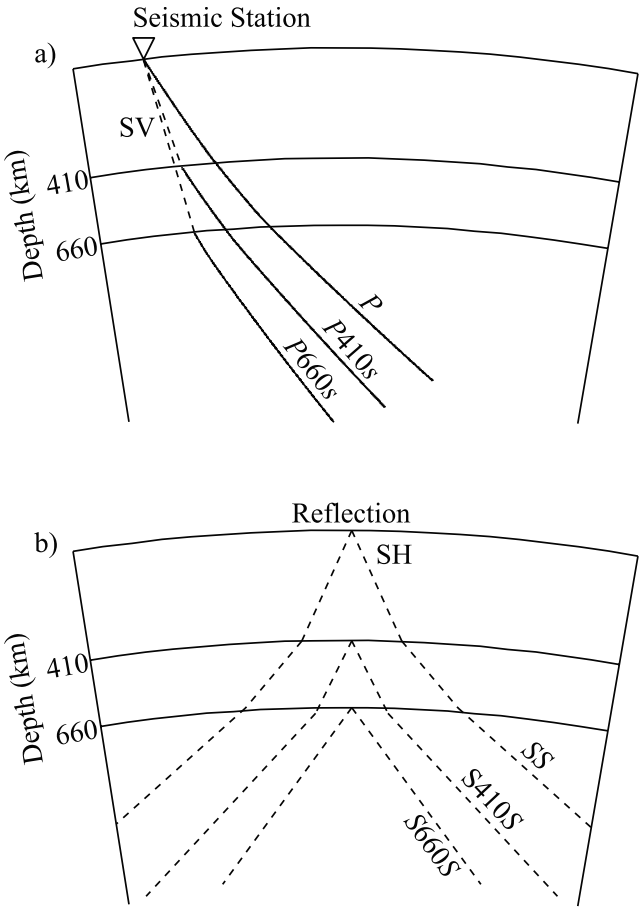

Figure 1. A graphical representation of (a) *Pds* waves and (b) *SdS* waves. Solid lines indicate compressional waves. Dashed lines indicate shear waves.

and Shearer, 1998; *Gu et al.*, 1998; *Gu and Dziewonski*, 2002] indicates that the results are robust. It is therefore puzzling that previous receiver function analyses have not shown very good agreement with these *SS* precursor results; this is one motivation for our study.

[6] *Pds* studies commonly focus on variations in transition zone structure on small lateral scales (hundreds of kilometers) beneath temporary seismic networks [e.g., *Vidale and Benz*, 1992; *van der Lee et al.*, 1994; *Yamazaki and Hirahara*, 1994; *Bostock*, 1996; *Shen et al.*, 1996; *Dueker and Sheehan*, 1997; *Shen et al.*, 1998; *Li et al.*, 2000; *Gilbert et al.*, 2003] rather than global studies [*Stammler et al.*, 1992; *Chevrot et al.*, 1999]. *Chevrot et al.* [1999] compared *Pds* data from 45 new measurements and 37 previously published measurements. The *Chevrot et al.* [1999] results indicate that the average transition zone thickness is ~250 km, and finds correlation rather than the expected decorrelation between the 410- and 660-km discontinuity depths.

[7] This study pursues several avenues to determine the source of the discrepancy between the patterns of global *SdS* and global *Pds* described by *Chevrot et al.* [1999]. First, we stack a global receiver function data set to produce a single composite receiver function, from which the 410- and 660-km discontinuity depths are calculated. Second, we stack the long-period receiver functions at each station separately to determine lateral variations from the mean. Third, we compare these new results to previous *SdS* studies and the *Pds* results of *Chevrot et al.* [1999]. Fourth, we discuss several causes of systematic error that explain the differences between this study and others.

2. Stacking

[8] With advances in modern computing and data availability, it is possible to evaluate thousands of seismograms in a matter of hours using automated methods. We analyze *Pds* for all high signal-to-noise global seismic data that fit the following two criteria from a database of over 300,000 long-period waveforms recorded between 1978 and 2002. (1) The event-to-station distance must fall within 30° and 90° to ensure steep incidence angles at the transition zone interfaces. Events closer than 30° are not steep enough to decouple shear and compressional impulses. Records from events farther than 90° become complicated because of vertical and lateral heterogeneity at the CMB. (2) After removing the instrument response, rotating the horizontal components into radial and tangential waveforms, and applying a Parzen band-pass filter between 0.01 and 0.2 Hz, the signal amplitude (the 60 s during and following the *P* wave onset) must be greater than twice the noise amplitude (the 60 s preceding the *P* wave onset). These requirements reduce our data set to ~30,000 waveforms.

[9] Before examining the receiver function stacks it is beneficial to first examine radial and vertical *P* waves. Prior to stacking, each record is normalized and time shifted relative to the maximum amplitude of the *P* wave. These normalized and time shifted records are stacked into 142 bins according to event-to-station distances between 25 to 96 degrees. The two-dimensional (2-D) *P* wave stacks are represented as blue (positive) and red (negative) on a color map of time versus distance (Figure 2). A nine-point moving average is applied to smooth the data, further reducing noise and making consistent phases more visible. The data are plotted in time relative to *P* wave arrival times. Coherent phases, such as *PP*, *PcP*, and *ScP*, are clearly visible on the stacked plots. On the vertical plot, phases such as *Pp*660*P*, the topside *P* wave reflection off of the "660," and *Pp*410*P* are visible. The radial *P* wave stack more clearly shows the *P*660*s* and *P*410*s* reflections. However, the source functions of the stacked *P* waves interfere with other phases within ±50 s, making direct evaluation of the *P*410*s* phase unstable.

[10] We stack receiver functions with the following method: (1) Each receiver function is calculated from the radial and vertical component waveform with spectral deconvolution [*Langston*, 1979]. Spectral deconvolution is very fast and works well for large quantities of coherent long-period data, so we prefer it over other more advanced and computationally expensive methods [e.g., *Gurrola and Minster*, 1998; *Park and Levin*, 2000]. Applying an acausal, low-pass filter and a waterlevel stabilizes the spectral division. (2) Each receiver function is normalized to unity by dividing the series by the maximum amplitude of the initial *P* wave peak. (3) Receiver functions are discarded if peaks having amplitudes greater than 10% of the maximum amplitude occur prior to the initial *P* wave peak. While no

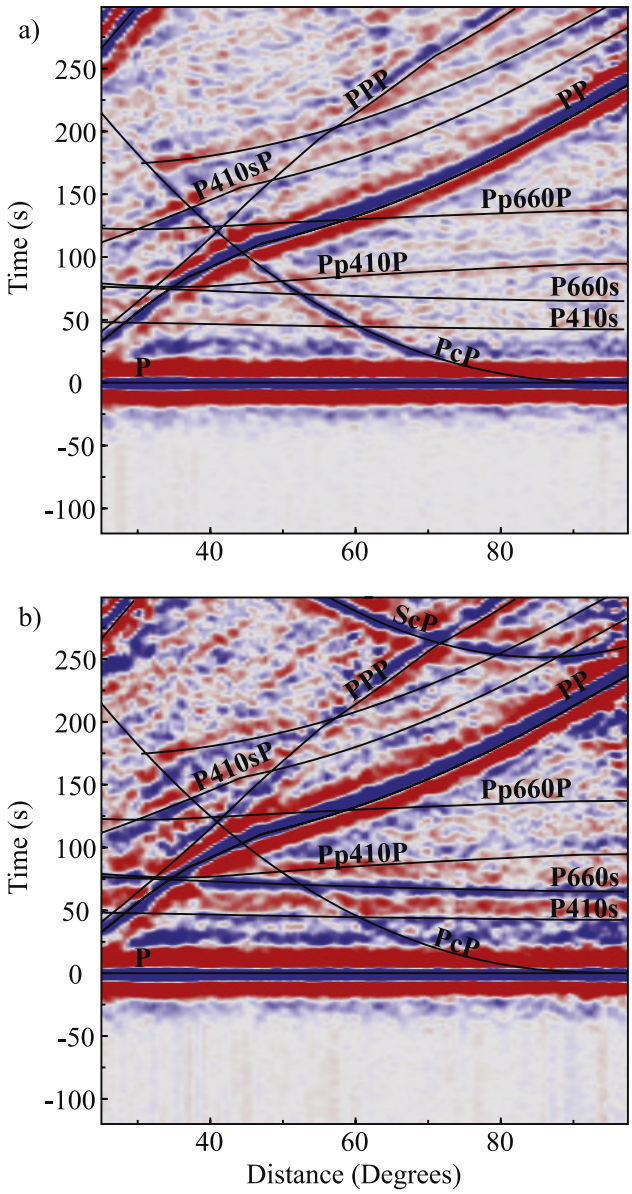

Figure 2. A two-dimensional (2-D) amplitude plot (time versus distance) of a *P* wave stack from 22,781 long-period seismograms for (a) vertical and (b) radial components. The color saturates at −0.15 (red) and 0.15 (blue). Black lines indicate the theoretical arrival times based on 20-s preliminary reference Earth model (PREM) [*Dziewonski and Anderson*, 1981].

phases should arrive prior to the initial *P* wave peak in the receiver function, unstable deconvolution often results in large amplitudes for this time window. This criterion ensures stability of deconvolution in a fast, automated scheme, necessary for processing thousands of waveforms. (4) The record is shifted so that the maximum amplitude of the initial *P* wave peak occurs at relative time zero. This largely removes shallow crustal and upper mantle contamination. (5) The receiver function is added to the 1° bin corresponding to its epicentral distance (with 61 bins spanning from 29.5° to 90.5°). (6) The resulting 61 stacked receiver functions are normalized to have unit amplitude at relative time zero. (7) Each of the stacked receiver functions is converted to depth at a 0.5 km sampling interval by using theoretical 20-s preliminary reference Earth model (PREM) [*Dziewonski and Anderson*, 1981] *Pds*-*P* times calculated in a spherical geometry. (8) These functions are integrated over event-to-station distance to obtain a single stacked depth-converted receiver function. The distance-integrated stack is evenly weighted for all distances because each bin is normalized to unity in step 5.

[11] The globally stacked receiver functions (Figure 3) reduce the dependence on the source function and crustal effects of the *P* wave, making the *P*410*s* and *P*660*s* arrivals more clearly visible. These *P*-to-*S* conversions match the predicted 20-s PREM traveltimes and move out for each phase (Figure 3a). By using the PREM predicted times, this moveout can be removed, resulting in a depth-corrected receiver function image (Figure 3b). Irregularities in the image of the 410- and 660-km phases result from interference from *PP* and *PcP*, as well as possible depth and/or brightness variations in the discontinuities. Integration over distance for each interpolated depth provides a single globally stacked receiver function as a function of depth (Figures 3c and 3d). The peak amplitudes of the depth-corrected *P*-to-*S* conversions occur at 406 km and 651.5 km, equating to a transition zone thickness of 246.5 km. However, we will show later this thickness estimate (which assigns all seismograms roughly equal weight) is larger than results obtained for a more spatially uniform global average. Lateral variations in discontinuity depths can be resolved by examining separate results for individual seismic stations. Examples of single-station 2-D and distance-integrated stacks for station CTAO are shown in Figure 4. Results are generally less coherent than the globally averaged results, reflecting the smaller number of stacked traces and the less complete distance coverage. Nevertheless, distinct *P*410*s* and *P*660*s* phases are apparent for most stations. For each station the depth versus distance receiver function image is stacked to yield individual depths for the 410- and 660-km discontinuities. These 118 individual station stacks are plotted in Figure 5.

3. Transition Zone Thickness

[12] The peaks in the integrated depth-converted receiver functions correspond to the depths of seismic velocity contrasts. In our global-scale analysis, the dominant signals are from the 410- and 660-km discontinuities. To minimize the errors in computed depths imposed by upper mantle and crustal structures, we examine the width of the transition zone (W_{TZ} = d660 − d410) rather than the calculated depths of the individual interfaces. Because both the *P410s* and *P660s* are nearly identically affected by lateral variations in crustal and upper mantle structure, the differencing of depths yields a more accurate result than the individual depths.

[13] An automated bootstrap resampling method is employed to estimate the error associated with the peak amplitude depths. Twenty integrated depth-converted receiver function stacks are calculated by randomly sampling the data. This yields twenty different transition zone thickness values for each stack. The standard deviation of these twenty transition zone thicknesses yields an estimate of the

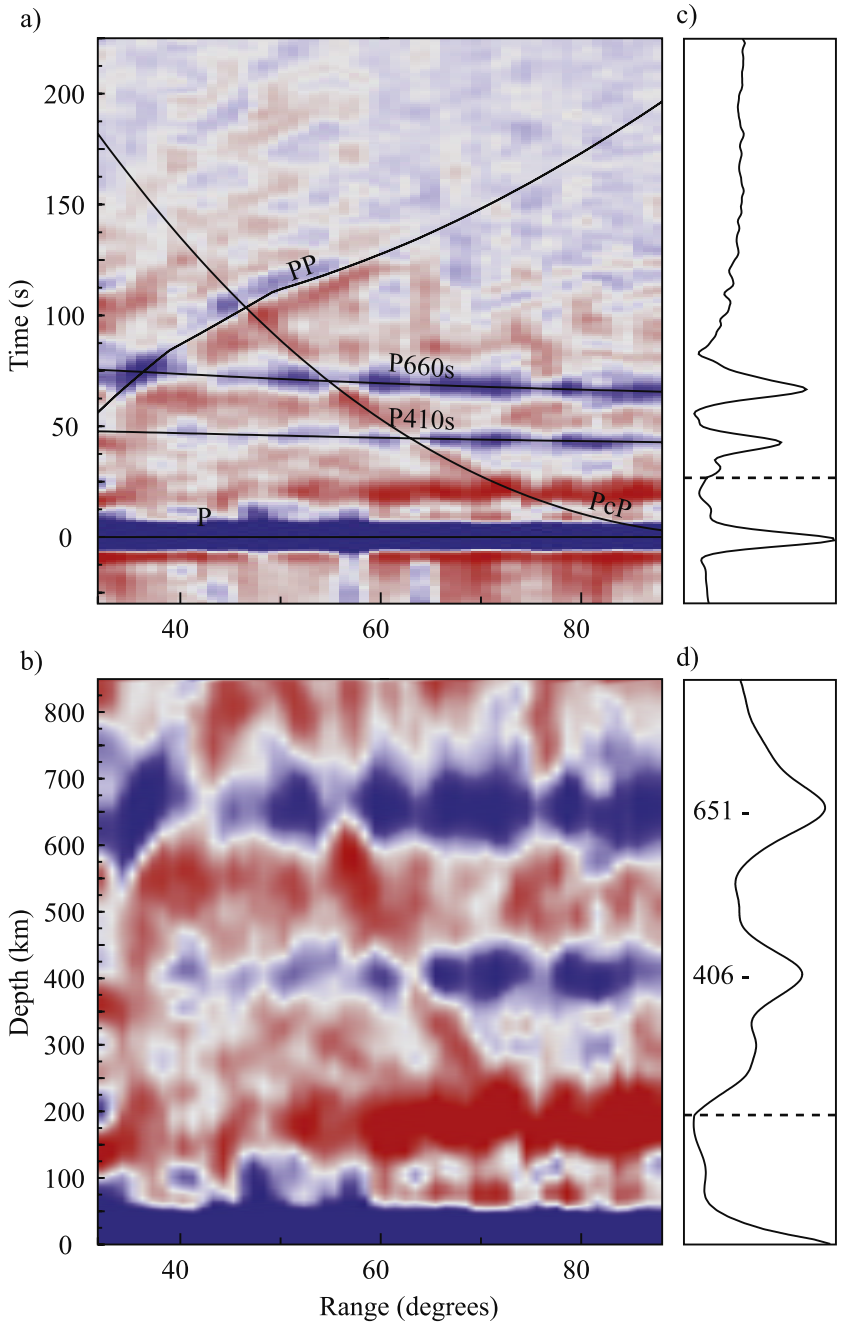

Figure 3. A 2-D global receiver function stack for 2841 seismograms plotted as a function of distance and (a) time or (b) computed depth. The color saturates at −0.1 (red) and 0.1 (blue). Black lines indicate the theoretical arrival times based on 20-s PREM [*Dziewonski and Anderson*, 1981]. The 1-D global stack is plotted as amplitude versus (c) time and (d) depth. The dashed lines in Figures 3c and 3d delineate an increase in amplitude magnification at later times by a factor of 10.

standard error of the depth estimate. This error estimation technique requires a large amount of data to provide stable error estimates, limiting the number of stations for which this process is applicable.

[14] The calculated transition zone thickness is dependent upon the velocity model used to determine the depths. The transition zone thickness is sensitive to velocity heterogeneity within the transition zone [e.g., *Ritsema et al.*, 2004]. Therefore, after stacking with PREM as the reference model [*Dziewonski and Anderson*, 1981], we apply a correction for each station because of velocity perturbations between 410 and 660 km, as determined by tracing the PREM ray path of *P660s* and *P410s* through the *S* wave model SB10L18 [*Masters et al.*, 2000] along the dominant ray parameter for each stack. While other seismic velocity models have higher resolution, this model was constructed by inverting simultaneously for *P* and *S* wave velocity perturbations. While higher resolution *P* and *S* wave tomography exists for

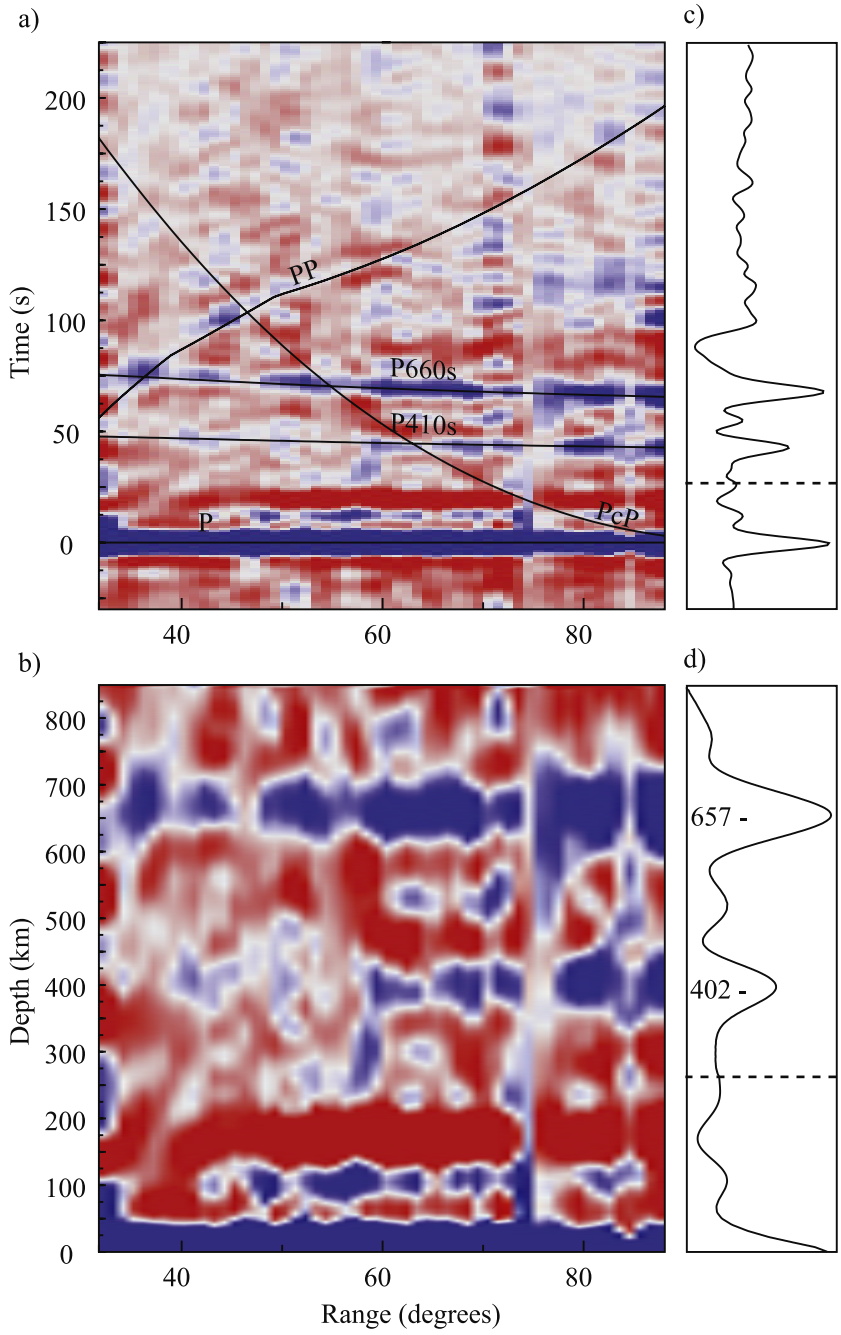

Figure 4. A 2-D receiver function stack for station CTAO plotted as a function of distance and (a) time or (b) computed depth. The color saturates at −0.1 (red) and 0.1 (blue). Black lines indicate the theoretical arrival times based on 20-s PREM. The 1-D CTAO stack is plotted as amplitude versus (c) time and (d) depth. The dashed lines in Figures 3c and 3d delineate an increase in amplitude magnification at later times by a factor of 10.

a few regional studies, we prefer to employ a velocity correction associated with a single model. The resulting velocity perturbations are largely less than ±1%, leading to corrections of less than ±2.5 km. We estimate that only very small errors (<1 km) are accumulated as a result of applying the 3-D velocity correction after stacking rather than prior to stacking. Corrections, based on other models, (e.g., S16B30 of *Masters et al.* [1996]) yield largely similar results even if assumptions regarding $\delta \ln V_P / \delta \ln V_S$ must be made. For brevity, the 118 corrected and uncorrected thicknesses values (W_{TZ}) are tabulated in the auxiliary material.[1]

[15] The global transition zone thickness varies on the order of ±20 km, with maximum perturbations of about ±35 km. The average of the individually calculated velocity-corrected transition zone thicknesses is 246.1 km,

[1] Auxiliary material is available at ftp://ftp.agu.org/apend/jb/2005jb003973.

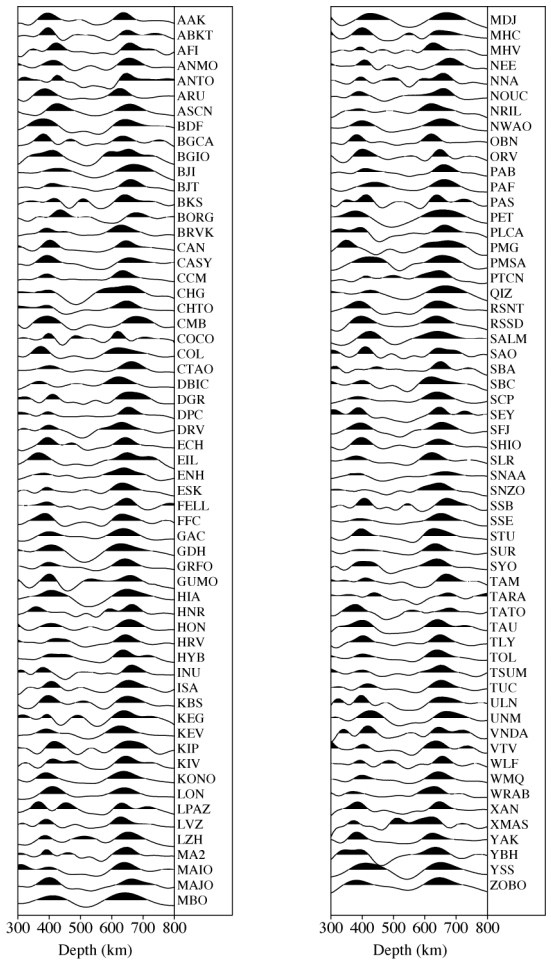

Figure 5. Distance-converted *Pds* stack for each of the 118 seismic stations examined in this study. Peak amplitudes are normalized to unity.

with a standard deviation of 14.1 km. The distribution of velocity-corrected transition zone thicknesses has a maximum at 242 ± 2 km depending on the bin size and choice of bin center locations. The median velocity-corrected W_{TZ} is 245.4 km. The distribution (quantified with a 5 km bin size and a 5 km step size) is illustrated in Figure 6.

4. Geographic Distribution

[16] The geographic distribution of transition zone thickness anomalies ($d_{TZ} = W_{TZ} - 246$ km) is depicted in Figure 7. Clearly coherent patterns of thick and thin d_{TZ} are visible on the global scale. Anomalously thick W_{TZ} is observed beneath eastern Asia and South America, where subduction is currently active. Thinner W_{TZ} is observed beneath the Pacific, Atlantic and Indian oceans. Applying a spherical Gaussian cap smoothing filter to the data (Figure 8) shows strong agreement with the *SS* precursor results of *Gu et al.* [1998] (hereinafter referred to as GDA98) and *Flanagan and Shearer* [1998] (hereinafter referred to as FS98). The Gaussian filter used here is similar to a scalable window degree-6 spherical harmonic low-pass filter [*Simons et al.*, 1997], which has the advantage of being more stable for unevenly sampled data. The smoothing process averages measurements that are close to each

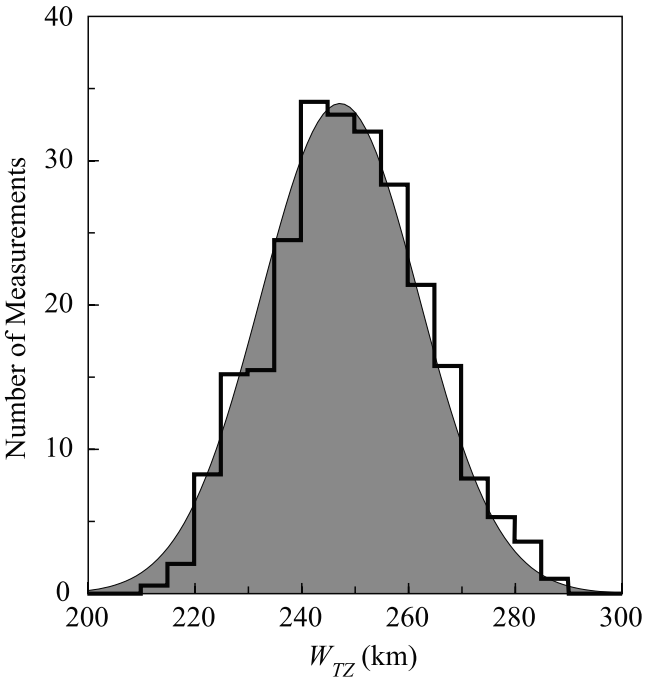

Figure 6. Distribution (black line) of *Pds* results and the best fitting normal distribution (shaded area).

other, but not those that are distant from each other. Consequently, the smooth model is not as biased by uneven geographic sampling. Once filtered, the laterally averaged transition zone thickness is W_{TZ} = 242 ± 2 km. This

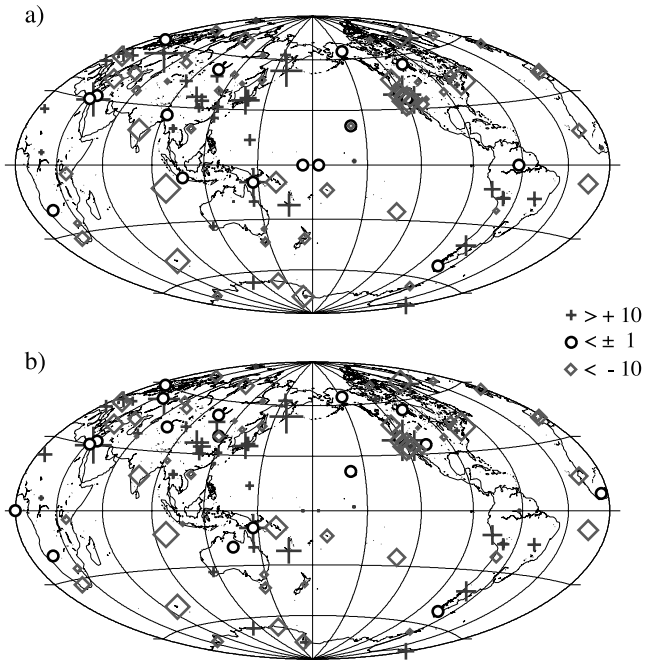

Figure 7. Maps of (a) the raw *Pds* transition zone thickness anomalies and (b) velocity perturbation–corrected *Pds* transition zone thickness anomalies relative to 246 km. Plus marks indicate thick transition zone; diamonds indicate thin transition zone, and black circles indicate no perturbation from 246 km.

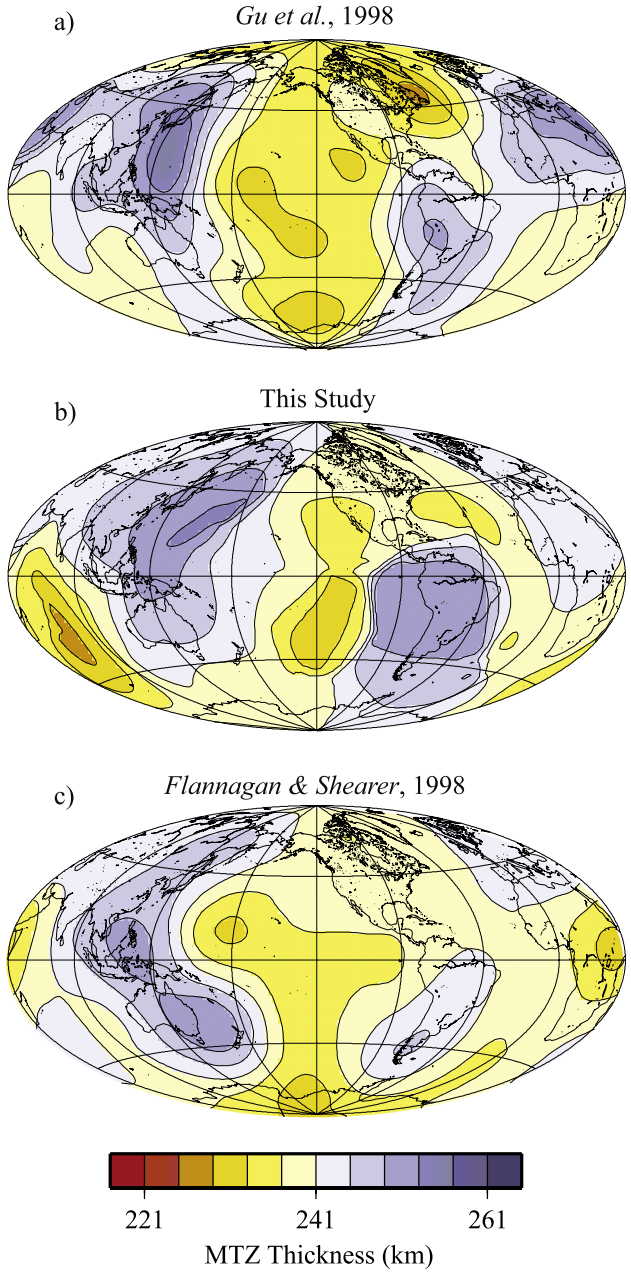

Figure 8. Smoothed maps of transition zone thickness for (a) *Gu et al.* [1998], (b) this study, and (c) *Flanagan and Shearer* [1998].

difference from the station average obtained above (W_{TZ} = 246 km) indicates that the geographic limitation in station locations causes oversampling of anomalously thick transition zone. Short-wavelength (tens to hundreds of kilometers) variations in transition zone thickness are observed among nearby stations, which have been observed in many previous studies [e.g., *Shen et al.*, 1998; *Gilbert et al.*, 2003].

[17] The *Pds* global topography model presented here is less robust than previous *SdS* models because of more irregular lateral coverage of the *Pds* results. We illustrate this by demonstrating that the *SdS* derived W_{TZ} model of FS98 fits both *SdS* and *Pds* results better than the *Pds* model (Table 1). Table 1 shows the RMS misfit for point-by-point comparison between the transition zone thickness measurements of the stacks and the long-wavelength ($l < 6$) transition zone thickness models for this study (hereinafter referred to as LS06) and FS98. Each set of stacks is compared with each long-wavelength model. The RMS misfit between the station *Pds* results and our smoothed W_{TZ} model is 12.5 km. The RMS misfit only increases by 5% when the *Pds* results are compared with FS98. By comparison, the RMS misfit between stacked *SdS* cap thicknesses and the smoothed FS98 model is only 10.6 km. The RMS misfit between observed *SdS* cap depths of *Flanagan and Shearer* [1998] increases by 46% when compared to the smoothed *Pds* model presented here. The smooth FS98 model fits both the *Pds* and *SdS* results more reasonably than the *Pds* smoothed model. Consequently we wish not to focus on the *Pds* model, but emphasize that the *SdS* models of *Flanagan and Shearer* [1998], *Gu et al.* [1998] and *Gu and Dziewonski* [2002] can reasonably explain the *Pds* data.

5. *Pds* Amplitudes

[18] The distance integrated global stack has *P*410*s* and *P*660*s* amplitudes that are 7.5% and 10.0% of the radial *P* wave amplitude, respectively. These amplitudes are remarkably similar to those of plane wave synthetic receiver functions created from IASPEI91 [*Kennett and Engdahl*, 1991], which provides amplitudes of 7.4% and 9.7% for *P*410*s* and *P*660*s* respectively assuming a Poisson's ratio of 0.25. While the *P*410*s* pulse has a similar shape to the initial radial *P* wave pulse, the *P*660*s* is asymmetrically broadened by ~10 s after the *P*660*s* peak. The globally stacked *P*520*s* is not detectable, either because of a low-amplitude interference from the *P*410*s* and *P*660*s*, or larger V_P contrast than V_S contrast. Phase stripping methods [e.g., *Shearer*, 1996] are made difficult because of the difference in shape between the *P*410*s* and the *P*660*s* phases.

[19] Individual distance integrated stacks for each seismic station have *P*410*s* and *P*660*s* amplitudes that range from 0% to 12.4% and 4% to 14.7% respectively. We considered *Pds* values with amplitudes less than 1% to be null results and did not measure W_{TZ} for these stations or include them in Table 1 or Figures 5–9. Observed *P*520*s* amplitudes range from 0% to 6%. A positive upswing near *P*520*s* was observed in 59% of the stacks where both *P*410*s* and *P*660*s* were identified. However, only ~40% of these potential *P*520*s* pulses are stable and have amplitudes above the noise level. *P*-to-*S* conversions from shallow interfaces (<250 km) are largely overpowered by crustal reverberations. The *PpSdp* and *PsPds* from the Moho cause the large negative pulse at ~20 s or ~200 km depth (Figures 3 and 4).

6. Discussion

[20] There does not appear to be a discrepancy between these *Pds* results and previous *SdS* results. While the

Table 1. RMS Misfit[a]

	LS06 *Pds* Model	FS98 *SdS* Model
LS06 *Pds* stacks	12.5	13.1
FS98 *SdS* caps	15.4	10.6

[a]LS06, this study; FS98, *Flanagan and Shearer* [1998].

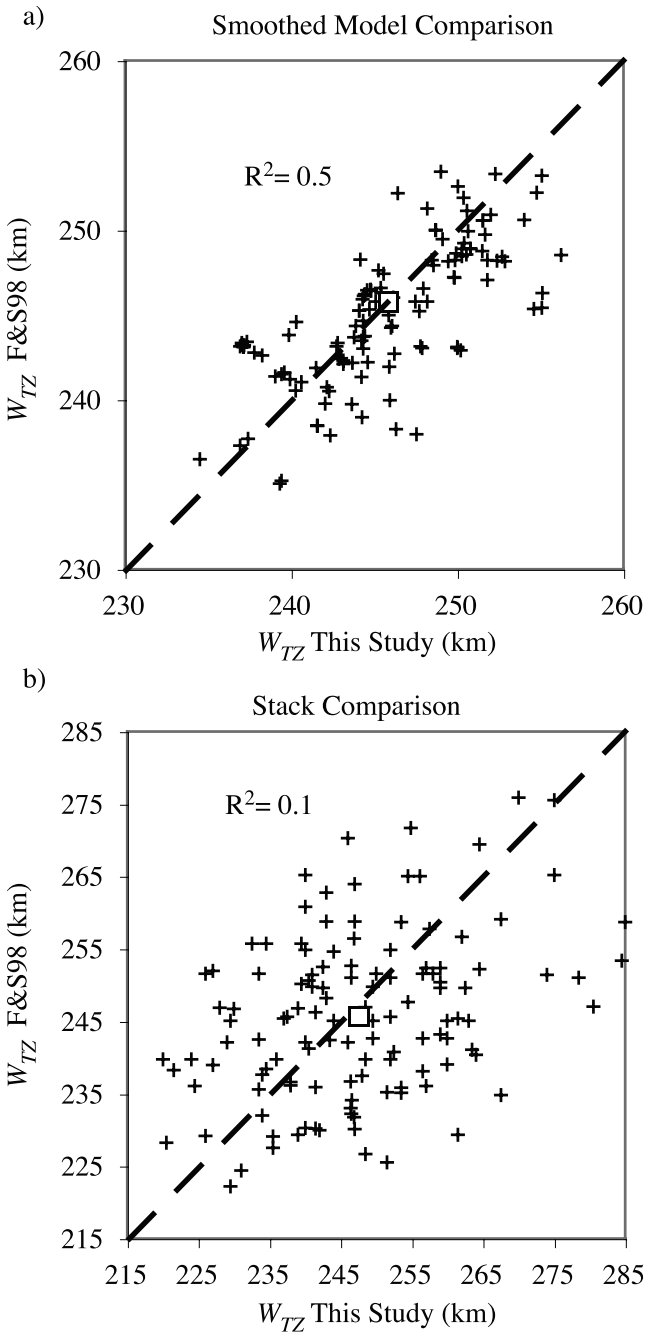

Figure 9. (a) Smoothed and (b) binned/stacked transition zone thicknesses of *Flanagan and Shearer* [1998] compared to those of this study. The Flanagan and Shearer results are sampled once for each of the 118 observed *Pds* measurements. The correlation of each comparison is given by R^2. The dashed line represents the expected relationship with a slope of unity. The squares represent the average values of each comparison.

average observed velocity-corrected *Pds* transition zone thicknesses (W_{TZ} = 246.1 km) is different from the average *SdS* transition zone thickness (W_{TZ} = 242 ± 2 km), it agrees better than *Chevrot et al.* [1999] (251 km). The limited geographic sampling of *Pds* measurements (particularly beneath oceans) likely causes the gap between our globally stacked transition zone thickness and those of *SS* precursor studies. These *Pds* measurements oversample thick regions and undersample thin regions because of the preferential locations of seismometers on land. The geographic average of long-wavelength smooth transition zone thickness from this study is 242 km (Figure 8). The low-passed geographic distribution of *Pds* thicknesses shows similar anomalous W_{TZ} locations and amplitudes to that of *SdS* studies. Geographically sampling the stacked and modeled W_{TZ} values of FS98 once at each location of *Pds* measurements provides a basis for direct comparison (Figure 9). Despite low correlation between stacked *SdS* and *Pds* measures of W_{TZ} (R^2 = 0.1), the mean values (W_{TZ} = 246.5 ± 1 km) are nearly identical. Considering that *Pds* fluctuations occur on much smaller scales, the low correlation is expected when comparing individual points. The smoothed models correlate much better (R^2 = 0.5) while maintaining nearly identical mean values (W_{TZ} = 245.5 ± 1 km). As illustrated above, the long-wavelength *SdS* model fits the *Pds* data nearly as well as the long-wavelength *Pds* model. Therefore the *Pds* data are consistent with *SdS* data where data exist. The *Pds* data preferentially sample thicker transition zone regions because of the predominance of seismometers on continents and the lack of seismometers in the oceans [*Gossler and Kind*, 1996].

[21] Owing to the uneven global resolution provided by *Pds* and similarity between these results and those of previous *SdS* studies we limit our interpretation of anomalous transition zone thickness and refer the reader to previous *SdS* studies [*Flanagan and Shearer*, 1998; *Gu et al.*, 1998; *Gu and Dziewonski*, 2002]. As we have shown here, there is no substantial discrepancy between *Pds* and *SdS* results, at least at long wavelengths, so future work may benefit from examining both *Pds* and *SdS* results in the same study.

[22] The ~5 km difference between average transition zone thickness values for this study and that of *Chevrot et al.* [1999], is mainly caused by the difference in stacking and time-to-depth conversion. As mentioned in the methods section, this study converts time to depth by interpolating between relative arrival times of *Pds-P* using a spherical geometry, allowing different ray parameters for *Pds* and *P*. *Chevrot et al.* [1999] employed the plane wave approximation of *Kind and Vinnik* [1988], which uses the same ray parameter for *P* and *Pds*. While the ray parameter varies only slightly between *P* and *Pds*, this can cause significant errors in conversion to depth. The plane wave approximation underestimates the theoretical traveltime difference between *Pds* and *P* (Figure 10). Stacking with underestimated moveout results in an overestimated relative time of the observed peak amplitude. This overestimated time results in an overestimated transition zone thickness. *Chevrot et al.* [1999] corrected moveout by referencing the ray parameter to 6.4 s deg^{-1} (or ~55° event-to-station distance), which causes a consistent 4-km overestimation of W_{TZ}.

[23] Our observed short-wavelength variations in measured transition zone thickness among nearby stations may be viewed in two lights; as either error or actual short-wavelength variations. In several respects the two are the same. Short-wavelength variations lead to less stable stacks because of stacking waveforms transmitted through tilted or

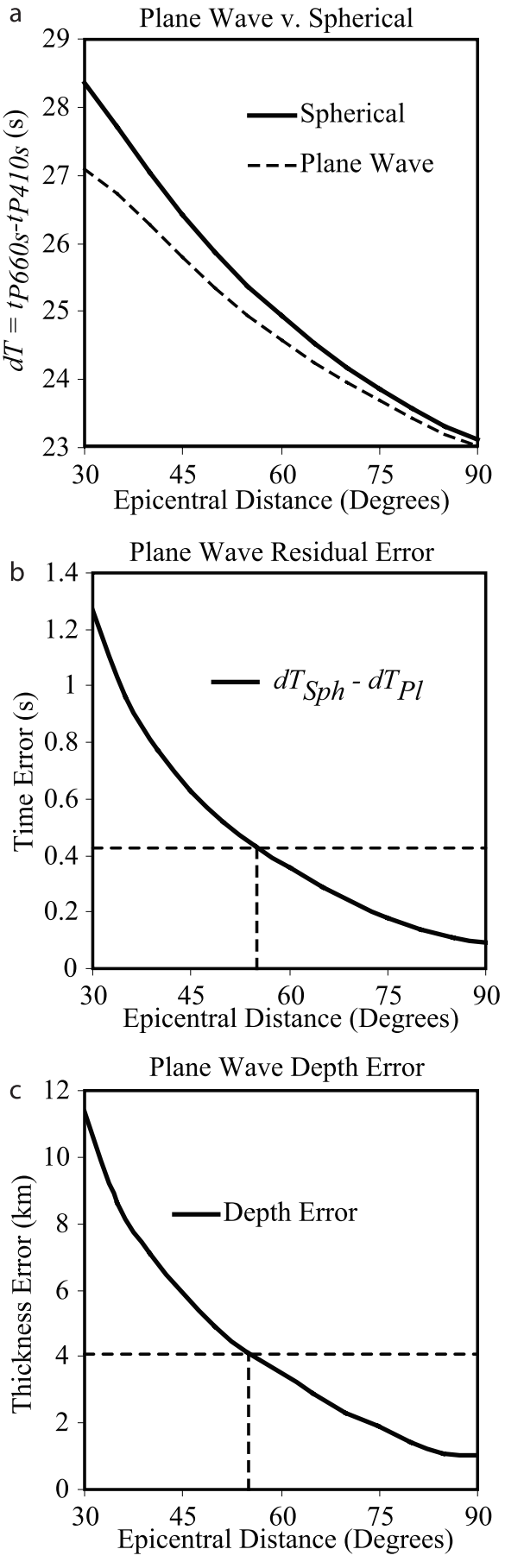

curved interfaces. In regions where the transition zone topography varies rapidly, the velocity likely also varies rapidly, resulting in erroneous time to transition zone thickness conversions. As *Li et al.* [2003] have shown, the general patterns of thick and thin transition zone agree between *SdS* and *Pds* results, but the short-wavelength amplitudes of transition zone thickness variation are greater for *Pds* (especially near mantle plumes). Consequently they argue that *SS* precursor data fail to observe the short-wavelength topography for plumes, and that *Pds* time variations likely require shorter-wavelength velocity corrections than are provided by current global seismic velocity models. The large circular areas used to stack sufficient *SS* data for stable stacks likely smoothes over topography, resulting in lower amplitudes. Nevertheless, the experimentally determined Clapeyron slopes of both discontinuities agree much better with *SdS* data than with *Pds* data [*Bina and Helffrich*, 1994; *Li et al.*, 2003], suggesting that the *SdS* data may be more robust.

[24] The estimated transition zone thickness depends on the reference velocity model used in the calculation. Changing the velocity model from PREM [*Dziewonski and Anderson*, 1981] to IASPEI91 [*Kennett and Engdahl*, 1991] causes ~1 km variation. Additional error may be incorporated in calculating transition zone thickness without accounting for 3-D velocity heterogeneity. A 2.5% positive velocity anomaly in the transition zone may result in a 6 km underestimation of transition zone thickness. However, accounting for velocity perturbations using the shear velocity models, SB10L18 [*Masters et al.*, 2000], S16B30 [*Masters et al.*, 1996] or SB4L18 [*Masters et al.*, 2000], does not significantly change the global pattern of *Pds* transition zone thicknesses. In general, one might expect thicker transition zones to result from colder temperatures and higher seismic velocities in the transition zone, and conversely for thinner transition zones to be associated with slower velocities. Such a correlation has been observed weakly for the global *SdS* studies [e.g., *Flanagan and Shearer*, 1998] and more strongly for particular regions by *Lebedev et al.* [2002, 2003]. For such correlated anomalies, the velocity heterogeneity correction largely makes thick transition zones thicker and thin transition zones thinner. The globally averaged net velocity corrections change the average transition zone thickness by less than 0.5 km.

7. Conclusion

[25] We stack receiver functions from global seismic stations to measure average transition zone thickness as well as the regional variations in transition zone thickness. The station-averaged observed transition zone thickness is 246 km but a more spatially uniform average yields 242 km, in good agreement with *SS* precursor studies. The long-wavelength global pattern and amplitude of transition zone

Figure 10. The plane wave approximation underestimates the (a) theoretical time delay between *Pds* and *P*, resulting in an over estimation of the (b) time delay anomaly and (c) transition zone thickness anomaly. The reference slowness used by *Chevrot et al.* [1999] corresponds to the depth error marked by the dashed line (4 km).

thickness variations are similar to those found by global *SdS* studies, indicating that no significant discrepancy exists between the *Pds* and *SdS* constraints on transition zone structure.

[26] **Acknowledgments.** This study was conducted with help and subroutines from Guy Masters and data from the Data Management Center of the Incorporated Research Institutions for Seismology. We thank Justin Revenaugh, Yu Jeffrey Gu, and an anonymous reviewer for their suggestions and comments. This research was supported by National Science Foundation grant EAR02-29323.

References

Ammon, C. J. (1991), The isolation of receiver effects from teleseismic *P* waveforms, *Bull. Seismol. Soc. Am.*, *81*, 2504–2510.

Ammon, C. J., G. E. Randall, and G. Zandt (1990), On the nonuniqueness of receiver function inversions, *J. Geophys. Res.*, *95*, 15,303–15,318.

Bina, C. R., and G. Helffrich (1994), Phase transition Clapeyron slopes and transition zone seismic discontinuity topography, *J. Geophys. Res.*, *99*, 15,853–15,860.

Bostock, M. G. (1996), *Ps* Conversions from the upper mantle transition zone beneath the Canadian landmass, *J. Geophys. Res.*, *101*, 8393–8402.

Chevrot, S., L. P. Vinnik, and J.-P. Montagner (1999), Global-scale analysis of the mantle *Pds* phases, *J. Geophys. Res.*, *104*, 20,203–20,219.

Dueker, K. G., and A. F. Sheehan (1997), Mantle discontinuity structure from midpoint stacks of converted P to S waves across the Yellowstone hot spot track, *J. Geophys. Res.*, *102*, 8313–8327.

Deuss, A. J., and J. H. Woodhouse (2001), Seismic observations of splitting of the mid-transition zone discontinuity in Earth's mantle, *Science*, *294*, 354–357.

Deuss, A. J., and J. H. Woodhouse (2002), A systematic search for mantle discontinuities using *SS*-precursors, *Geophys. Res. Lett.*, *29*(8), 1249, doi:10.1029/2002GL014768.

Dziewonski, A. M., and D. Anderson (1981), Preliminary reference Earth model, *Phys. Earth Planet. Inter.*, *25*, 297–356.

Flanagan, M. P., and P. M. Shearer (1998), Global mapping of topography on transition zone velocity discontinuities by stacking *SS* precursors, *J. Geophys. Res.*, *103*, 2673–2692.

Gilbert, H. J., A. F. Sheehan, K. G. Dueker, and P. Molnar (2003), Receiver functions in the western United States, with implications for upper mantle structure and dynamics, *J. Geophys. Res.*, *108*(B5), 2229, doi:10.1029/2001JB001194.

Gossler, J., and R. Kind (1996), Seismic evidence for very deep roots of continents, *Earth Planet. Sci. Lett.*, *138*, 1–13.

Gu, Y. J., and A. M. Dziewonski (2002), Global variability of transition zone thickness, *J. Geophys. Res.*, *107*(B7), 2135, doi:10.1029/2001JB000489.

Gu, Y. J., A. M. Dziewonski, and C. B. Agee (1998), Global de-correlation of the topography of transition zone discontinuities, *Earth Planet. Sci. Lett.*, *157*, 57–67.

Gurrola, H., and J. B. Minster (1998), Thickness estimates of the upper-mantle transition zone from bootstrapped velocity spectrum stacks of receiver functions, *Geophys. J. Int.*, *133*, 31–43.

Jackson, I. (1983), Some geophysical constraints on the chemical composition of the Earth's lower mantle, *Earth Planet. Sci. Lett.*, *62*, 143–164.

Katsura, T., and E. Ito (1989), The system Mg_2SiO_4–Fe_2SiO_4 at high pressures and temperatures: Precise determination of stabilities of olivine, modified spinel, and spinel, *J. Geophys. Res.*, *94*, 15,663–15,670.

Kennett, B. L. N., and E. R. Engdahl (1991), Traveltimes for global earthquake location and phase identification, *Geophys. J. Int.*, *105*, 113–130.

Kind, R., and L. P. Vinnik (1988), The upper mantle discontinuities underneath the GRF array from *P*-to-*S* conversed phases, *Geophys. J.*, *62*, 138–147.

Langston, C. A. (1979), Structure under Mount Rainier, Washington, inferred from teleseismic body waves, *J. Geophys. Res.*, *84*, 4749–4762.

Lebedev, S., S. Chevrot, and R. D. Van der Hilst (2002), Seismological constraints on the origin of the 410- and 660-kilometer discontinuities, *Science*, *296*, 1300–1302.

Lebedev, S., S. Chevrot, and R. D. Van der Hilst (2003), Effective Clapeyron slopes of the 410 and 660 km discontinuities beneath Australia and eastern Asia, *Phys. Earth Planet. Inter.*, *136*, 25–40.

Lee, D.-K., and S. Grand (1996), Depth of upper mantle discontinuities beneath the East Pacific Rise, *Geophys. Res. Lett.*, *23*, 3369–3372.

Li, A., K. M. Fischer, M. E. Wysession, and T. J. Clarke (1998), Mantle discontinuities and temperature under the North American continental keel, *Nature*, *395*, 160–163.

Li, X., S. V. Sobolev, R. Kind, X. Yuan, and C. H. Estabrook (2000), A detailed receiver function image of the upper mantle discontinuities in the Japan subduction zone, *Earth Planet. Sci. Lett.*, *183*, 527–541.

Li, X., R. Kind, X. Yuan, S. V. Sobolev, W. Hanka, D. S. Ramesh, Y. Gu, and A. M. Dziewonski (2003), Seismic observation of narrow plumes in the oceanic upper mantle, *Geophys. Res. Lett.*, *30*(6), 1334, doi:10.1029/2002GL015411.

Masters, G., S. Johnson, G. Laske, and H. Bolton (1996), A shear-velocity model of the mantle, *Philos. Trans. R. Soc. London, Ser. A*, *354*, 1385–1411.

Masters, G., G. Laske, H. Bolton, and A. Dziewonski (2000), The relative behavior of shear velocity, bulk sound speed, and compressional velocity in the mantle: Implications for chemical and thermal structure, in *Earth's Deep Interior: Mineral Physics and Tomography from the Atomic to the Global Scale*, *Geophys. Monogr. Ser.*, vol. 117, edited by S. Karato et al., pp. 63–87, AGU, Washington D. C.

Park, J., and V. Levin (2000), Receiver functions from multiple-taper spectral correlation estimates, *Bull. Seismol. Soc. Am.*, *90*, 1507–1520.

Petersen, N., L. P. Vinnik, G. Kosarev, R. Kind, S. Oreshin, and K. Stammler (1993), Sharpness of the mantle discontinuities, *Geophys. Res. Lett.*, *20*, 859–862.

Ringwood, A. E. (1975), *Composition and Petrology of the Earth's Mantle*, 618 pp., McGraw-Hill, New York.

Ritsema, J., H. J. Van Heijst, and J. H. Woodhouse (2004), Global transition zone tomography, *J. Geophys. Res.*, *109*, B02302, doi:10.1029/2003JB002610.

Shearer, P. M. (1991), Constrains on upper mantle discontinuities from observations of long-period reflected and converted phases, *J. Geophys. Res.*, *96*, 18,147–18,182.

Shearer, P. M. (1993), Global mapping of upper mantle reflectors from long period *SS* precursors, *Geophys. J. Int.*, *115*, 878–904.

Shearer, P. M. (1996), Transition zone velocity gradients and the 520-km discontinuity, *J. Geophys. Res.*, *101*, 3053–3066.

Shearer, P. M., and G. Masters (1992), Global mapping of topography on the 660-km discontinuity, *Nature*, *355*, 791–796.

Shearer, P. M., M. P. Flanagan, and M. A. H. Hedlin (1999), Experiments in migration processing of SS precursor data to image upper mantle discontinuity structure, *J. Geophys. Res.*, *104*, 7229–7242.

Shen, Y., S. C. Solomon, I. T. Bjarnason, and G. M. Purdy (1996), Hot mantle transition zone beneath Iceland and the adjacent Mid-Atlantic Ridge inferred from *P*-to-*S* conversions and the 410- and 660-km discontinuities, *Geophys. Res. Lett.*, *23*, 3527–3530.

Shen, Y., A. F. Sheehan, K. G. Dueker, C. de Groot-Hedlin, and F. Gilbert (1998), Mantle discontinuity structure beneath the southern East Pacific Rise from *P*-to-*S* converted phases, *Science*, *280*, 1232–1235.

Simons, M., S. C. Solomon, and B. H. Hager (1997), Localization of gravity and topography: Constraints on the tectonics and mantle dynamics of Venus, *Geophys., J. Int.*, *131*, 24–44.

Stammler, K., R. Kind, N. Petersen, L. P. Vinnik, and L. Qiyuan (1992), The upper mantle discontinuities correlated or anticorrelated?, *Geophys. Res. Lett.*, *19*, 1563–1566.

van der Lee, S., H. Paulssen, and G. Nolet (1994), Variability of *P*660*s* phases as a consequence of topography of the 660 km discontinuity, *Phys. Earth Planet. Inter.*, *86*, 147–164.

Vidale, J. E., and H. M. Benz (1992), Upper-mantle seismic discontinuities and the thermal structure of subduction zones, *Nature*, *356*, 678–683.

Vinnik, L. P. (1977), Detection of waves converted from *P* to *SV* in the mantle, *Phys. Earth Planet. Inter.*, *15*, 39–45.

Vinnik, L. P., G. Kosarev, and N. Petersen (1996), Mantle transition zone beneath Eurasia, *Geophys. Res. Lett.*, *23*, 1485–1488.

Yamazaki, A., and K. Hirahara (1994), The thickness of upper mantle discontinuities, as inferred from short-period J-Array data, *Geophys. Res. Lett.*, *21*, 1811–1814.

Yuen, D. A., D. M. Reuteler, S. Balachandar, V. Steinbach, A. V. Malevsky, and J. J. Smedsmo (1994), Various influences on three-dimensional mantle convection with phase transitions, *Phys. Earth Planet. Inter.*, *86*, 185–203.

J. F. Lawrence and P. M. Shearer, Institute of Geophysics and Planetary Physics, Scripps Institution of Oceanography, 9500 Gilman Drive, La Jolla, CA 92093-0225, USA. (jlawrence@ucsd.edu)